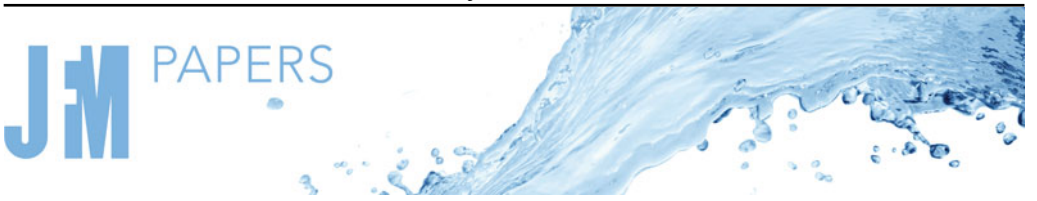
J. Fluid Mech. (2026), *vol.* 1042, A26, doi:10.1017/jfm.2026.11999



Validity of the twin-force analogy in Couette flows

Zhouxin Jiang[1,2,3], **Shengqi Zhang**[2,3], **Jiaao Hao**[1], **Chao Sun**[4,5], **Zhiyang Cai**[2,3,6] **and Zhijian Wang**[2,3]

[1]Department of Aeronautical and Aviation Engineering, The Hong Kong Polytechnic University, Hong Kong SAR, PR China

[2]Zhejiang Key Laboratory of Industrial Intelligence and Digital Twin, Eastern Institute of Technology, Ningbo 315200, PR China

[3]Ningbo Key Laboratory of Advanced Manufacturing Simulation, Eastern Institute of Technology, Ningbo 315200, PR China

[4]Center for Combustion Energy, Key Laboratory for Thermal Science and Power Engineering of MoE, and Department of Energy and Power Engineering, Tsinghua University, Beijing 100084, PR China

[5]Department of Engineering Mechanics, School of Aerospace Engineering, Tsinghua University, Beijing 100084, PR China

[6]School of Ocean and Civil Engineering, Shanghai Jiao Tong University, Shanghai 200240, PR China

Corresponding author: Shengqi Zhang, szhang@eitech.edu.cn

(Received 4 March 2026 UTC; revised 25 June 2026 UTC; accepted 30 July 2026 UTC)

This study combines linear stability analysis (LSA) and direct numerical simulations (DNS) to investigate the coupling mechanisms of rotation, stratification and shear in two flow geometries: spanwise rotating stratified plane Couette flow (between two infinite parallel plates) and sheared annular centrifugal Rayleigh–Bénard convection (between two concentric cylinders). First, LSA reveals a universal scaling law with respect to $(1-\eta)$, where η denotes the radius ratio, for the deviation between annular and planar system results, quantitatively establishing the dynamical connection between annular and planar geometries. Building on this, DNS results indicate that the breakdown of the twin-force analogy in the turbulent regime originates from mode competition: buoyancy tends to drive three-dimensional chaotic plumes via baroclinic effects, whereas the Coriolis force tends to sustain quasi-two-dimensional longitudinal vortices. The Prandtl number determines the dominant mechanism in the near-wall region by regulating the relative thicknesses of the thermal and momentum boundary layers, thereby leading to a systematic dissimilarity between heat and momentum transport. Furthermore, this study provides a new theoretical basis for transport prediction in complex flows from the perspectives of enstrophy and mode competition.

Key words: stratified turbulence, rotating turbulence, instability

© The Author(s), 2026. Published by Cambridge University Press.

https://doi.org/10.1017/jfm.2026.11999 Published online by Cambridge University Press

1. Introduction

The coupling effects of rotation, shear and stratification constitute a core physical problem in wall-bounded turbulence, with relevance to atmospheric science, astrophysics and turbomachinery (Deardorff 1972; Wyngaard 1992; Hartmann *et al.* 2001; Young & Read 2017; Feng *et al.* 2022). Buoyancy-driven Rayleigh–Bénard convection (RBC) and rotation-driven Taylor–Couette flow (TCF) serve as classical paradigms for studying heat and momentum transport, respectively. In RBC, the fluid motion is driven by buoyancy. Its flow stability and scalar transport (Nu) are primarily influenced by the Rayleigh number (Ra) and the Prandtl number (Pr), leading to the relevant scaling laws relating Nu, Pr and Ra (Grossmann & Lohse 2001; Ahlers *et al.* 2009). Conversely, in TCF, the shear-driven turbulence generated by the rotation of the inner and outer cylinders has its stability and momentum transport influenced by the rotation number and geometric factors (Yoshikawa *et al.* 2013; Grossmann *et al.* 2016; Zhong *et al.* 2023, 2024). Current research findings, particularly theoretical work based on the framework of Grossmann & Lohse (2001, 2002), have revealed profound physical similarities in the transport scaling laws of these two systems (Grossmann *et al.* 2016). Busse (2012) astutely pointed out that this similarity constitutes the theoretical cornerstone for studying rotation and stratification effects.

This physical similarity facilitated the proposal of the twin-force analogy theory, which reveals a profound intrinsic similarity between the Coriolis force generated by rotation and the buoyancy force generated by density stratification, providing a novel theoretical perspective for the unified analysis of turbulence under these coupled multiphysics fields (Busse 2012; Zhang & Sun 2024). For instance, by establishing a strict mathematical analogy between two-dimensional–three-component rotating shear flow and thermal convection problems, the theoretical analysis of flow instability can be significantly simplified, leading to the derivation of generalised solutions (Zhang *et al.* 2019). An ideal platform for validating this analogy is the spanwise rotating stratified plane Couette flow (RSPCF). As a classical model for studying the coupling of shear, rotation and stratification, it possesses unique realistic significance in geophysical contexts. Given that the planetary boundary layer is locally best approximated as a planar system, RSPCF provides an ideal planar physical framework for capturing atmospheric 'cloud streets'. As pointed out by Etling & Brown (1993), cloud streets originate from the combined effects of dynamic and thermal instabilities, which is precisely the core dynamic mechanism in RSPCF that organises turbulence into quasi-two-dimensional large-scale structures. From the perspective of theoretical limits, RSPCF is also regarded as the theoretical limit of sheared annular centrifugal RBC (ACRBC) as the curvature approaches zero (Faisst & Eckhardt 2000; Dou *et al.* 2008; Brauckmann *et al.* 2016, 2017; Kang *et al.* 2019; Eckhardt *et al.* 2020; Zhong *et al.* 2024). This is crucial for validating the twin-force analogy in rotating systems, because the presence of curvature in ACRBC can obscure the effects of the Coriolis force, whereas in RSPCF, we can strictly isolate the Coriolis force and draw a corresponding mathematical analogy with buoyancy effects. Furthermore, Zhang & Sun (2024) found that at $Pr = 1$ under pure system rotation, RSPCF induces large-scale flow structures similar to those driven by pure stratification; this structural similarity serves as the physical basis for the analogy study. Notably, in ACRBC, the imposition of shear can completely stabilise the flow, a phenomenon that does not occur in classical three-dimensional wall-sheared RBC. This highlights the decisive role of rotation (Coriolis force): it effectively suppresses the spanwise instability that dominates in planar geometries (Zhong *et al.* 2023).

Therefore, one of the primary objectives of this paper is to quantitatively verify the theoretical connection between ACRBC and RSPCF over a more comprehensive

https://doi.org/10.1017/jfm.2026.11999 Published online by Cambridge University Press

parameter range via linear stability analysis (LSA), thereby providing a solid theoretical basis for generalising planar flow theories, such as the twin-force analogy, to more complex curved systems. Establishing this geometric representativeness is a prerequisite for generalisability: only by confirming the representativeness of RSPCF geometrically can the mechanism of analogy breakdown found in RSPCF be confidently extrapolated to practical curved flows such as ACRBC. Previous studies have provided key insights into the flow structure and transport mechanisms of RSPCF, but have also revealed a fundamental paradox. On the one hand, as mentioned above, the large-scale streamwise roll structures are topologically similar to thermal convection rolls, constituting the physical cornerstone of the 'twin-force analogy' at $Pr = 1$ (Zhang & Sun 2024). However, on the other hand, this structural similarity does not guarantee transport similarity. Brethouwer (2021) showed that rotation can cause heat/mass transport to become much faster than conventional momentum transport in Couette flows. This decoupling of transport mechanisms leads to the failure of the classical Reynolds analogy (Brethouwer 2018, 2021, 2023). Zhang & Sun (2024) proposed a modified inertial-frame Reynolds analogy, and preliminarily verified its applicability at $Pr = 1$ and for some parameters where $Pr \neq 1$.

Consequently, the second primary objective of this paper is to build upon this foundation by extending the validation of this inertial-frame Reynolds analogy to a broader parameter space using direct numerical simulations (DNS), with a specific focus on the physical mechanisms underlying its breakdown. We will reveal that the fundamental differences between the twin forces – buoyancy and the Coriolis force regarding vorticity generation and the sustenance of turbulent modes in three-dimensional space – are the core reasons leading to the systematic breakdown of this analogy when $Pr \neq 1$. The present work builds on Zhang & Sun (2024), which established the twin-force framework mainly in planar Couette turbulence, and focused on the approximate similarity of turbulent transport. The present study extends this framework in two directions. First, we use LSA to quantify the asymptotic connection between ACRBC and RSPCF as the curvature decreases, including the $(1-\eta)$ scaling of the critical parameters (where η denotes the radius ratio), and how the stability boundary is determined by the competition between different two-dimensional flow modes. Second, we use DNS to examine the limitations and breakdown mechanisms of the analogy through global Richardson number $Ri_\chi = 0$ cases, different values of Pr, and energy/enstrophy and spectral analyses. Thus the present study not only connects the planar twin-force framework to a curved annular system, but also clarifies why the analogy can fail in nonlinear turbulent transport.

The remainder of this paper is organised as follows. Section 2 introduces the governing equations, physical models and numerical methods. Section 3 presents the LSA and establishes the asymptotic connection between ACRBC and RSPCF. Section 4 then examines nonlinear turbulent transport and flow structures in RSPCF using DNS. Finally, conclusions are given in § 5.

2. Physical model and numerical methods

2.1. *Governing equations and system definition*

This study investigates two typical wall-bounded turbulent systems: sheared ACRBC and spanwise RSPCF. In the RSPCF system, as shown in figure 1(*a*), the fluid is confined between two infinite parallel plates separated by a gap width L. The unit vectors of the x-, y- and z-axes are denoted by $\hat{\boldsymbol{x}}$, $\hat{\boldsymbol{y}}$ and $\hat{\boldsymbol{z}}$, respectively. The top and bottom walls move with equal and opposite velocities, creating a background shear with streamwise velocity

https://doi.org/10.1017/jfm.2026.11999 Published online by Cambridge University Press

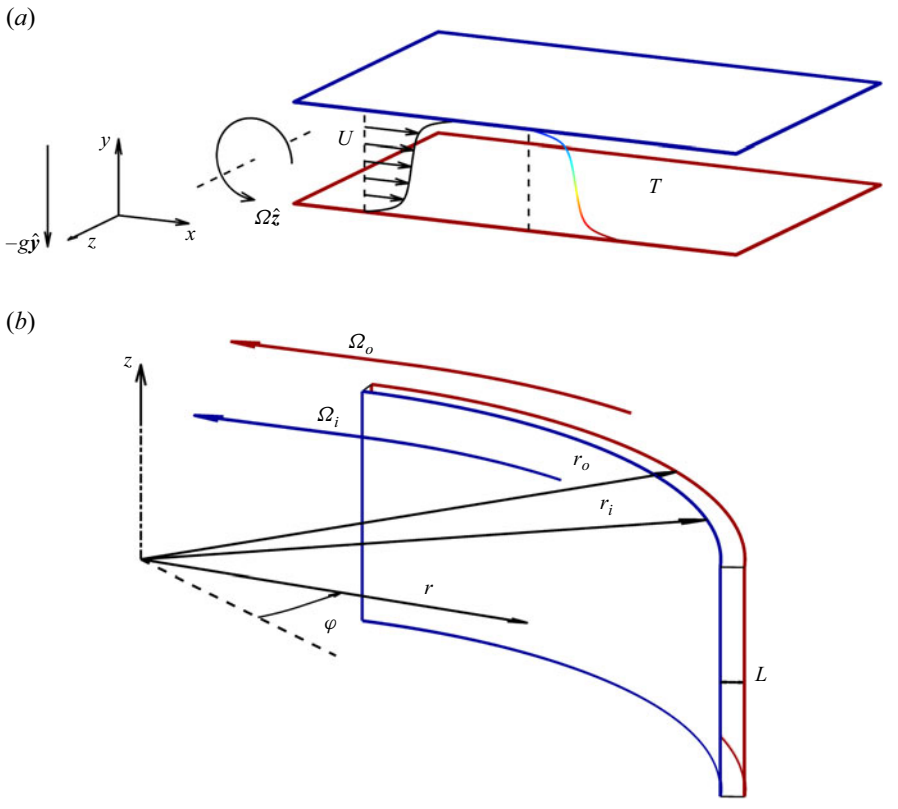


Figure 1. (*a*) Sketch of spanwise RSPCF. (*b*) Sketch of sheared ACRBC at large radius ratio.

difference $[U]$. The entire system rotates about the spanwise z-axis with angular velocity Ω, and is subject to gravitational acceleration $-g\hat{\boldsymbol{y}}$ acting in the negative y-direction. A temperature difference $[T]$ is maintained between the top and bottom walls. The velocity difference is adopted as the velocity reference scale. The non-dimensionalised governing equations are

$$\boldsymbol{\nabla}\cdot\boldsymbol{u}=0, \tag{2.1a}$$

$$\frac{\partial \boldsymbol{u}}{\partial t}+\boldsymbol{u}\cdot\boldsymbol{\nabla}\boldsymbol{u}=-\boldsymbol{\nabla}p+\frac{1}{Re}\nabla^2\boldsymbol{u}+R_\Omega\boldsymbol{u}\times\hat{\boldsymbol{z}}+\frac{Ra}{Re^2Pr}T\hat{\boldsymbol{y}}, \tag{2.1b}$$

$$\frac{\partial T}{\partial t}+\boldsymbol{u}\cdot\boldsymbol{\nabla}T=\frac{1}{RePr}\nabla^2T. \tag{2.1c}$$

Here, the boundary conditions are $\boldsymbol{u}|_{y=\pm0.5}=\pm0.5\hat{\boldsymbol{x}}$ and $T|_{y=\pm0.5}=\mp0.5$, with periodic boundary conditions applied in both the x- and z-directions.

For the ACRBC system, illustrated in figure 1(*b*), the unit vectors for r, φ, z are $\hat{\boldsymbol{r}}$, $\hat{\boldsymbol{\varphi}}$, $\hat{\boldsymbol{z}}$, respectively. An incompressible fluid is confined between two independently rotating coaxial cylinders with inner and outer radii r_i and r_o, respectively. The angular velocities of the inner and outer cylinders are $\Omega_i\hat{\boldsymbol{z}}$ and $\Omega_o\hat{\boldsymbol{z}}$, respectively. The mean angular velocity is defined as $\Omega=(\Omega_i+\Omega_o)/2$, and the radius ratio is $\eta=r_i/r_o$. The inner and outer cylinder walls are maintained at constant temperatures T_i and T_o, respectively, with temperature difference $[T]=T_o-T_i$. In this system, the centrifugal force field generated

https://doi.org/10.1017/jfm.2026.11999 Published online by Cambridge University Press

by the mean rotation provides an equivalent radial gravity. The linear velocity difference between the inner and outer cylinders, $[U]$, serves as the velocity reference scale, and $L = r_o - r_i$ is the gap width. As indicated by Zhang *et al.* (2022), the buoyancy effect caused by the inertial term $\boldsymbol{u}\cdot\boldsymbol{\nabla}\boldsymbol{u}$ cannot be approximated by an explicit momentum source term with $O(\alpha_T[T])$ relative error. Therefore, for simplicity, a valid buoyancy correction is not included in this work. The non-dimensionalised momentum equation for the ACRBC system is

$$\frac{\partial \boldsymbol{u}}{\partial t} + \boldsymbol{u}\cdot\boldsymbol{\nabla}\boldsymbol{u} = -\boldsymbol{\nabla} p + \frac{1}{Re}\nabla^2\boldsymbol{u} + R_\Omega \boldsymbol{u}\times\hat{\boldsymbol{z}} - T\frac{Ra}{Re^2 Pr}\frac{2(1-\eta)}{1+\eta}\hat{\boldsymbol{r}}. \tag{2.2}$$

Here, the velocity vector is $\boldsymbol{u} = (u_r, u_\varphi, u_z)$. The no-slip and isothermal boundary conditions are given by:

$$\text{for } r = r_i = \frac{\eta}{1-\eta}, \quad \boldsymbol{u} = \left(0, \frac{r_i}{r_o + r_i}, 0\right), \quad T = -0.5; \tag{2.3a}$$

$$\text{for } r = r_o = \frac{1}{1-\eta}, \quad \boldsymbol{u} = \left(0, \frac{-r_o}{r_o + r_i}, 0\right), \quad T = 0.5. \tag{2.3b}$$

Here, the domain is infinite in the axial direction.

The two systems share some common definitions of non-dimensional parameters, involving the kinematic viscosity ν, thermal diffusivity κ, and thermal expansion coefficient α_T of the fluid. The primary independent control parameters are defined as follows: Reynolds number $Re = [U]L/\nu$, rotation number $R_\Omega = 2\Omega L/[U]$, Rayleigh number $Ra = g\alpha_T[T]L^3/(\nu\kappa)$, and Prandtl number $Pr = \nu/\kappa$. Correspondingly for RSPCF, the thermal Nusselt number and the rotating-frame momentum Nusselt number are defined as $Nu_T = -\mathrm{d}\langle T\rangle/\mathrm{d}y\big|_{\pm 0.5}$ and $Nu_U = \mathrm{d}\langle U\rangle/\mathrm{d}y\big|_{\pm 0.5}$, respectively, where $\langle\cdot\rangle$ denotes averaging over time and the horizontal plane.

2.2. *Twin-force analogy and inertial-frame Reynolds analogy*

To unify the analysis and quantitative description of the coupling effects of rotation (Coriolis force) and stratification (buoyancy) in wall-bounded turbulence, we draw upon and extend the theoretical framework proposed by Zhang & Sun (2024). The core of this framework lies in revealing the profound similarity between Coriolis and buoyancy effects, and systematically describing their coupling through two central concepts: the twin-force analogy and the inertial-frame Reynolds analogy. This framework introduces a variable transformation $\theta = (R_\Omega y - u)/(1 - R_\Omega)$, and defines the inertial-frame momentum Nusselt number as $Nu_\theta = -\mathrm{d}\langle\theta\rangle/\mathrm{d}y\big|_{\pm 0.5}$, thereby absorbing the influence of rotation. Hereafter, the classical Reynolds analogy refers to the similarity between Nu_U and Nu_T, whereas the inertial-frame Reynolds analogy refers to that between Nu_θ and Nu_T. Consequently, the streamwise momentum equation can be rewritten in a form similar to the temperature transport equation; this transformation reveals that the action of the Coriolis force on the wall-normal velocity is analogous to a buoyancy effect, thus mathematically establishing the connection between these two forces. On this basis, to unify the quantification of rotation and stratification effects, the following non-dimensional parameters are introduced: the Coriolis Richardson number $Ri_\theta = R_\Omega(1 - R_\Omega)$, and the Coriolis Rayleigh number $Ra_\theta = Re^2 Ri_\theta$, where, under the present sign convention, positive Ra_θ corresponds to destabilising rotation, and negative Ra_θ corresponds to stabilising rotation. The relationship between the rotation number R_Ω and the Coriolis

https://doi.org/10.1017/jfm.2026.11999 Published online by Cambridge University Press

Rayleigh number is given by

$$R_\Omega = \frac{1}{2} \pm \sqrt{\frac{1}{4} - \frac{Ra_\theta}{Re^2}}, \tag{2.4}$$

where the solutions correspond to the strong and weak rotation regimes, respectively. The buoyancy Richardson number is defined as $Ri_T = Ra/Re^2$ for $Pr \leqslant 1$, and $Ri_T = Ra\,Pr/Re^2$ for $Pr > 1$, and the global Richardson number is $Ri_\chi = Ri_\theta + Ri_T$. In the Rayleigh number formulation used for the LSA, the global Rayleigh number is defined as $Ra_\chi = Ra_\theta + Ra$ without Pr correction. Two relative strength parameters, $\gamma = (Ri_T - Ri_\theta)/(Ri_T + Ri_\theta)$ and $\lambda = (Ra - Ra_\theta)/(Ra + Ra_\theta)$, are used to describe the relative contributions of buoyancy and the Coriolis force in Richardson number and Rayleigh number forms, respectively. Here, $\gamma = -1$ and $\lambda = -1$ represent pure rotation, whereas $\gamma = 1$ and $\lambda = 1$ represent pure stratification. Correspondingly, a global Nusselt number Nu_χ is defined as the weighted average of the heat and inertial-frame momentum transport coefficients:

$$Nu_\chi = \frac{1+\lambda}{2} Nu_T + \frac{1-\lambda}{2} Nu_\theta, \tag{2.5}$$

which is consistent with the calculated data in Zhang & Sun (2024). Based on this, the core idea of the twin-force analogy is proposed: buoyancy and the Coriolis force act as 'twin forces', whose effects on the flow field can be linearly superimposed or counteracted. Therefore, the overall transport efficiency of the system, Nu_χ, is primarily determined by the Reynolds number Re and the global Richardson number Ri_χ, showing weak dependence on the relative strength of the two effects. In previous studies at $Pr = 1$, the similarity between TCF and RBC in two dimensions was strictly proven through reasonable mathematical transformations (Tanaka *et al.* 2000; Zhang *et al.* 2019). Although explicit correspondence based on the original variables is incomplete in three-dimensional flows (Jeganathan *et al.* 2023), the inertial-frame Reynolds analogy based on the θ transformation has been verified for specific γ at $Pr = 1$. However, the combined effects of buoyancy and the Coriolis force on the flow still require verification for cases with $Pr = 1$ (specifically $Ri_\chi = 0$) and $Pr \neq 1$. Therefore, this study will systematically investigate these key parameter ranges via DNS to reveal the core laws that characterise the coupling of multiphysics involving rotation, stratification and shear.

2.3. *The LSA*

We employ LSA to quantitatively establish the theoretical connection between ACRBC and RSPCF at the critical point of instability. The relevant physical quantity $\tilde{\psi}$ is decomposed into the sum of a steady base flow Ψ_0 and an infinitesimal perturbation $\hat{\psi}$. For the ACRBC system, we adopt the LSA framework detailed in Zhong *et al.* (2023). For the RSPCF system, perturbations are imposed on the linear base flow $U_0(y) = y$ and $T_0(y) = -y$. Its governing equations can be simplified by introducing the wall-normal vorticity $\varpi = \partial u/\partial z - \partial w/\partial x$, yielding the following system of equations (Wallin *et al.* 2013):

$$s\varpi = -\mathrm{i}\alpha U_0 \varpi + \frac{1}{Re}\left(\mathrm{D}^2 - k^2\right)\varpi - \mathrm{i}\beta\left(U_0' - R_\Omega\right)v, \tag{2.6a}$$

$$s\left(\mathrm{D}^2 - k^2\right)v = -\mathrm{i}\alpha U_0\left(\mathrm{D}^2 - k^2\right)v + \frac{1}{Re}\left(\mathrm{D}^2 - k^2\right)^2 v - \mathrm{i}\beta R_\Omega \varpi - \frac{Ra}{Re^2 Pr}k^2 T, \tag{2.6b}$$

https://doi.org/10.1017/jfm.2026.11999 Published online by Cambridge University Press

$$sT = \left(-\mathrm{i}\alpha U_0 + \frac{\mathrm{D}^2 - k^2}{Re\,Pr}\right) T - v\mathrm{D}T_0. \tag{2.6c}$$

The boundary conditions are $y = \pm 0.5$, $v = \partial v/\partial y = \varpi = 0$. Here, $\mathrm{D} = \mathrm{d}/\mathrm{d}y$, and $k^2 = \alpha^2 + \beta^2$, with $\hat{\psi} = \psi(y)\,\mathrm{e}^{st+\mathrm{i}(\alpha x+\beta z)}$, where α and β are the streamwise and spanwise wavenumbers, respectively, and s is the complex growth rate. The governing equations of both systems constitute a generalised eigenvalue problem. We solve them numerically using the Chebyshev spectral collocation method.

2.4. *Numerical methodology*

To quantitatively validate our hypothesis under more complex conditions, DNS were performed using the open-source spectral element code NEK5000. The computational configuration largely follows Zhang & Sun (2024), with the parameters selected as $Re \in \{5000, 10\,000\}$, $Pr \in \{1, 4, 0.25\}$, $Ri_\chi \in \{0, 0.16\}$ and $\gamma \in \{0, \pm 1, \pm 2\}$. Notably, we have supplemented the study with a series of specific cases at $Ri_\chi = 0$, where the Coriolis and buoyancy forces exhibit identical magnitudes but act with opposing physical effects. These cases provide a crucial baseline for a detailed analysis of the superposition and cancellation mechanisms between the two forces. The computational domain has dimensions $L_x \times L_y \times L_z = 9\pi \times 1 \times 4\pi$, and the spectral element mesh consists of $N_x \times N_y \times N_z = 81 \times 10 \times 72$ elements. The polynomial order of the spectral elements was $N = 7$, corresponding to $N + 1 = 8$ Gauss–Lobatto–Legendre points in each spatial direction within each element.

Consistent with the LSA, the DNS employ no-slip isothermal walls and periodic boundary conditions in the horizontal directions. The grid resolution strictly follows the standards validated in Zhang & Sun (2024), ensuring sufficient accuracy for the current parameter space.

3. Linear stability: asymptotic connection between ACRBC and RSPCF

As demonstrated by the numerical verification of rotating shear flow in Brauckmann *et al.* (2016), plane Couette flow serves as the theoretical limit of TCF as the curvature vanishes. This study extends this concept to the ACRBC system by incorporating buoyancy effects, providing a critical pathway for generalising theories established in planar geometries – such as the twin-force analogy in spanwise RSPCF – to more universal curved geometric systems.

We begin with the LSA equation system (2.6) to derive two physically significant critical instability modes: stationary ($\mathrm{Im}[s] = 0$) and oscillatory ($\mathrm{Im}[s] \neq 0$). The governing equations for oscillatory and streamwise inhomogeneous conditions are presented in (3.1) below. Equation (3.1) is obtained by expressing T and ϖ in terms of v from (2.6*a*) and (2.6*c*), respectively, and substituting the resulting expressions into (2.6*b*). In the limit of streamwise homogeneity $\alpha = 0$, the equations corresponding to oscillatory and stationary modes reduce to (3.2*a*) and (3.2*b*), respectively (see below). It is observed that Pr continues to influence the critical parameters for oscillatory modes (3.2*a*). In contrast,when the instability is dominated by streamwise-uniform stationary rolls, the Prandtl number vanishes from the stability criterion (3.2*b*). Consequently, for stationary and streamwise-uniform conditions $s = 0$, $\alpha = 0$, the flow stability is independent of Pr. In this LSA section, the relative weighting between buoyancy and Coriolis branches is described by the Rayleigh-based parameter λ, whereas γ is reserved for the Richardson-based framework used in the nonlinear DNS discussion. This theoretical deduction aligns well with current numerical findings: the critical global Rayleigh number $Ra_{\chi,c}$ in the

https://doi.org/10.1017/jfm.2026.11999 Published online by Cambridge University Press

RSPCF system remains invariant across different Pr values. We have

$$\begin{aligned} 0 = &\left((\alpha U_0 - \mathrm{i}s)\left(\mathrm{D}^2 - k^2\right) + \frac{\mathrm{i}}{Re}\left(\mathrm{D}^2 - k^2\right)^2 \right) v \\ &- \beta^2 \frac{1-\lambda}{2} \frac{Ra_\chi}{Re^2} \left(\alpha U_0 - \mathrm{i}s + \frac{\mathrm{i}}{Re}\left(\mathrm{D}^2 - k^2\right) \right)^{-1} v \\ &- k^2 \frac{1+\lambda}{2} \frac{Ra_\chi}{Re^2 Pr} \left(\alpha U_0 - \mathrm{i}s + \frac{\mathrm{i}}{RePr}\left(\mathrm{D}^2 - k^2\right) \right)^{-1} v, \end{aligned} \tag{3.1}$$

$$Ra_\chi\, \beta^2 v = \left(-\frac{1-\lambda}{2}\frac{1}{Re^2}A - \frac{1+\lambda}{2}\frac{1}{Re^2 Pr}B \right)^{-1} \left(s\left(\mathrm{D}^2 - \beta^2\right) - \frac{1}{Re}\left(\mathrm{D}^2 - \beta^2\right)^2 \right) v, \tag{3.2a}$$

$$0 = \mathrm{i}(\mathrm{D}^2 - \beta^2)^2 v + \mathrm{i}\beta^2\, Ra_\chi \left(\mathrm{D}^2 - \beta^2\right)^{-1} v, \tag{3.2b}$$

where $A = [s - (\mathrm{D}^2 - \beta^2)/Re]^{-1}$ and $B = [s - (\mathrm{D}^2 - \beta^2)/(Re\, Pr)]^{-1}$.

Multiplying (3.2*b*) by $(\mathrm{D}^2 - \beta^2)/\mathrm{i}$ gives

$$\left(\mathrm{D}^2 - \beta^2\right)^3 v + \beta^2 Ra_\chi\, v = 0. \tag{3.3}$$

Under the same no-slip and isothermal boundary conditions, this is identical to the classical stationary Rayleigh–Bénard stability equation (Chandrasekhar 1961). Hence for the stationary streamwise-uniform branch, $Ra_{\chi,c}$ equals the critical Ra for RBC, and the critical wavenumber and eigenfunction are identical to those of classical RBC. Since λ, Pr and Re do not appear in this eigenvalue problem, $Ra_{\chi,c}$ is independent of these parameters. Next, to systematically verify the convergence of ACRBC to RSPCF as the radius ratio η tends to 1, we investigated a wide range of parameters. Here, the comparison of growth rates is used only as an auxiliary diagnostic of the linear-response convergence at a fixed Ra under the corresponding parameter and wavenumber mappings. The primary stability comparison is based on the critical Rayleigh number, whereas the growth-rate comparison further tests whether ACRBC and RSPCF exhibit consistent disturbance-amplification rates under the same supercritical forcing. The relative strength of rotation and stratification is quantified by the parameter λ. Figure 2(*a*) shows the relationship between $(1-\eta)$ and the relative difference of the growth rates $S = \mathrm{Re}[s]$ of the two systems under identical control parameters. Here, k_φ and k_z denote the azimuthal and spanwise wavenumbers of the ACRBC system, respectively. The relationship between k_φ and the streamwise wavenumber of the RSPCF system is given by $\alpha = k_\varphi/((r_o + r_i)/2)$. Under this parameter mapping, the relative difference exhibits a linear scaling in the small curvature limit:

$$\frac{|S_r^{ACRBC} - S_r^{RSPCF}|}{S_r^{RSPCF}} \propto (1-\eta). \tag{3.4}$$

This indicates that under various variations of control parameters, the ACRBC system gradually approaches the RSPCF system as η increases. Moreover, it can be seen from figure 2(*a*) that at high rotation numbers, the effect of geometric curvature is weakened, leading to behaviour closer to RSPCF (Brauckmann *et al.* 2016). Meanwhile, the linear stability results also reveal another universal quadratic scaling law. At $Pr = 1$, as shown in figure 2(*b*), under various combinations of rotation and stratification intensities, the relative difference of the critical global Rayleigh number $Ra_{\chi,c}$ between the two systems follows

https://doi.org/10.1017/jfm.2026.11999 Published online by Cambridge University Press

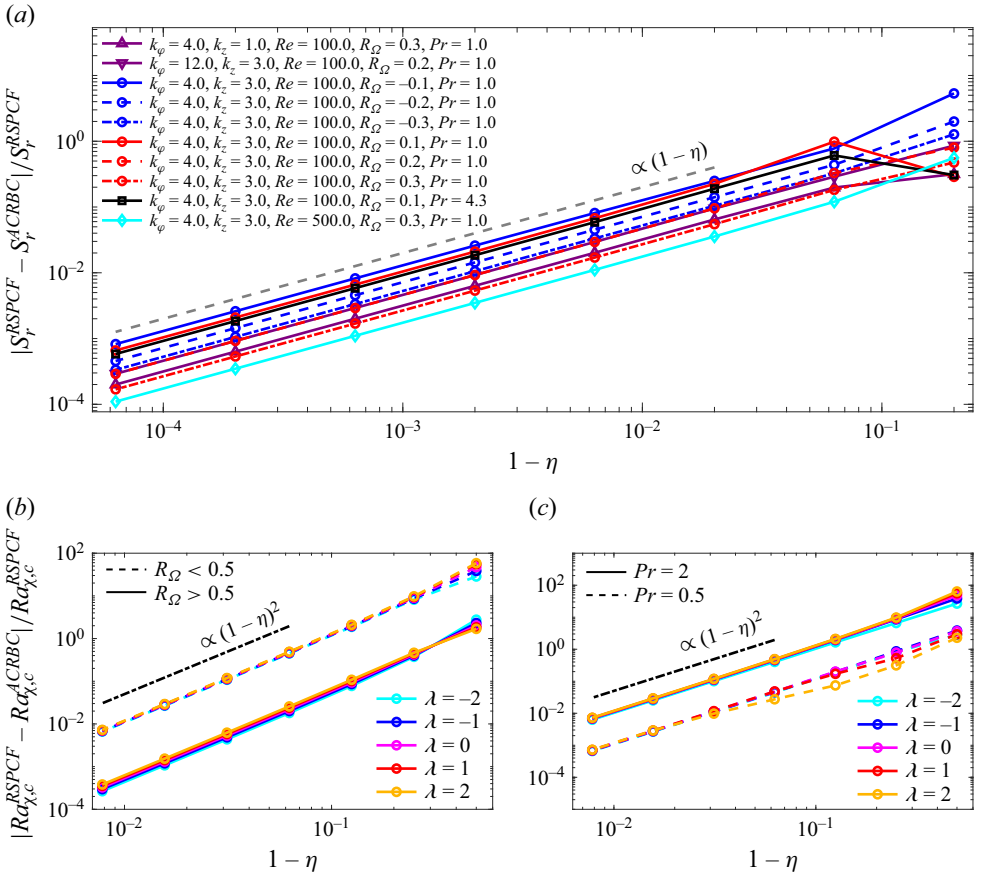


Figure 2. Convergence analysis and scaling law verification of instability parameters for ACRBC and RSPCF systems. (*a*) Variation of the relative difference of growth rates between ACRBC and RSPCF with $(1-\eta)$ under different parameters at $Ra = 10^5$. (*b*,*c*) The relative difference of $Ra_{\chi,c}$ between the two systems versus $(1-\eta)$ under mixed stratification and rotation at $Re = 200$ for $Pr = 1$ and $Pr = 0.5$, 2, respectively, where the results for $R_\Omega < 0.5$ in (*b*) and $Pr = 2$ in (*c*) are shifted upwards by 10 units.

$$\frac{|Ra_{\chi,c}^{ACRBC} - Ra_{\chi,c}^{RSPCF}|}{Ra_{\chi,c}^{RSPCF}} \propto (1-\eta)^2. \tag{3.5}$$

The universality of this scaling law is manifested in several aspects. First, the relationship holds for different relative strengths of rotation and stratification effects, and the curves for different λ nearly coincide, although the finite-curvature corrections may retain some dependence on λ. Second, considering the significant dynamical differences between the strong- and weak-rotation branches, with $R_\Omega > 0.5$ and $R_\Omega < 0.5$, respectively, we verified these two conditions separately under the same restrictive conditions. Here, the weak/strong rotation distinction refers to the two branches of $Ri_\theta = R_\Omega(1 - R_\Omega)$, not to a restriction to positive R_Ω. Therefore, the parameter space considered here includes both positive and negative R_Ω, although the present study does not aim to construct a separate cyclonic/anticyclonic regime map. The results show that this scaling law holds in both physical states (figure 2*b*). The discovery of the scaling law related to $(1-\eta)$ not only echoes that RSPCF is the asymptotic limit of ACRBC as η approaches 1, but also quantitatively describes how the influence of curvature, as a perturbation term, on system

https://doi.org/10.1017/jfm.2026.11999 Published online by Cambridge University Press

stability vanishes as $(1-\eta)$ decreases. Moreover, our numerical results indicate that $Ra_{\chi,c}$ for the RSPCF is independent of λ, which confirms the validity of the twin-force analogy. Therefore, we verified the universality of the twin-force analogy.

Zhang & Sun (2024) found that in the nonlinear regime with $Pr \neq 1$, the twin-force analogy is satisfied under certain γ. Since Pr has a significant influence on heat and momentum transport, we extend the analysis to $Pr \neq 1$ to observe its effect on linear stability. We calculated the variation of the relative difference of $Ra_{\chi,c}$ between the two systems with λ at Pr equal to 0.5 and 2, and found that in the linear stability region of different Pr, $Ra_{\chi,c}$ of RSPCF is independent of Pr and λ, and is equal to the critical value $Ra_{c,0}$, the critical Rayleigh number for the classical non-rotating RBC, thereby validating the twin-force analogy. This numerical result finds theoretical support from (3.2). When $\mathrm{Im}[s]=0$, $\alpha=0$, Pr has no effect on the flow. Under the same conditions, the ACRBC system exhibits stability similar to RSPCF only when the radius ratio η approaches 1 (figures 2*b*,*c*), with the lowest relative difference of the critical parameters currently calculated reaching $O(10^{-4})$. When η is small, its critical value varies significantly with λ. These results effectively broaden the applicable range of the twin-force analogy, enabling more efficient prediction of critical parameters under different fluid properties.

Different rotation and shear intensities have a significant impact on the flow state. With increasing shear, wall-sheared RBC is divided into buoyancy-dominated, transition and shear-dominated regimes (Hathaway & Somerville 1986; Blass *et al.* 2020). To comprehensively understand the coupling of shear, rotation and stratification in RSPCF, we examined two idealised two-dimensional flow limits separately, and linked them to the full three-dimensional instability characteristics. Figure 3 reveals that the stability boundary of the three-dimensional system is determined by the competition between two distinct two-dimensional physical mechanisms in parameter space.

The transition between the two two-dimensional modes can be systematically studied by increasing the shear Reynolds number Re at fixed values of the Coriolis contribution, $Ra_\theta = -10^1$, -10^3 and -10^5. Figure 3(*a*) can be interpreted as the competition between two critical thresholds. The x–y branch with $\beta \approx 0$ is insensitive to Ra_θ, because the Coriolis-force term vanishes for this mode, but it is stabilised by the background shear as Re increases. In contrast, the y–z branch with $\alpha \approx 0$ is almost insensitive to Re, but its threshold is determined by the stabilising Coriolis contribution associated with negative Ra_θ, because buoyancy must compensate for the stabilising Coriolis contribution.

In the low-Re region, the x–y branch has a lower critical threshold than the competing y–z branch. This is because the shear stabilisation of the x–y branch is still relatively weak, whereas negative Ra_θ shifts the threshold of the competing y–z branch upwards. Consequently, the primary instability mode manifests as spanwise vortices ($\beta \approx 0$) (as shown in figure 3*b*). Under this mechanism, background shear exerts a stabilising effect on the flow. As shown in figure 3(*a*), in the logarithmic plot, the increment of the critical Rayleigh number clearly exhibits a first linear region, with a slope corresponding to a quadratic scaling law:

$$Ra_c - Ra_{c,0} \propto Re^2. \tag{3.6}$$

It is worth noting that for this pure spanwise vortex mode with $\beta = 0$, the Coriolis force term plays no role in the linear stability equations; therefore, the critical curves under different background rotation intensities coincide completely with the results of the two-dimensional x–y plane in this linear interval. The physical mechanism can be attributed to the background shear stretching the convective vortex structures in the streamwise direction, thereby inhibiting vertical heat transport (Goluskin *et al.* 2014; Blass *et al.* 2020). However, the shear stabilisation raises the threshold of the x–y branch,

https://doi.org/10.1017/jfm.2026.11999 Published online by Cambridge University Press

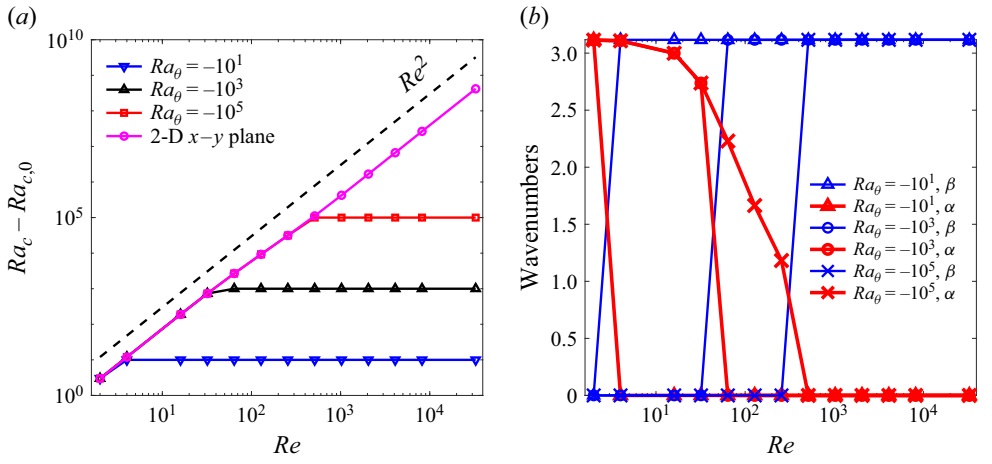


Figure 3. Influence of different rotation and shear intensities on wavenumbers. (*a*) Effect of shear on critical Ra. (*b*) Variation of streamwise wavenumber (α) and spanwise wavenumber (β) with different shear intensities.

and the instability mode shifts to be dominated by streamwise vortices ($\alpha \approx 0$) (as shown in figure 3*b*). For this mode, background shear has almost no effect. Consequently, in figure 3(*a*), the critical curve enters a second linear region, indicating that the critical parameter $Ra_c - Ra_{c,0}$ asymptotically approaches a constant independent of Re, with a value equal to $-Ra_\theta$.

In summary, the selection between the spanwise- and streamwise-vortex modes is governed by the competition between the shear-stabilised x–y branch and the y–z branch whose threshold is modified by the Coriolis contribution. The x–y branch is mainly controlled by Re and is insensitive to Ra_θ, whereas the y–z branch is controlled by Ra_θ and is almost insensitive to Re. This indicates that the stability boundary of the three-dimensional system is determined by the competition between two distinct two-dimensional physical mechanisms in parameter space. Combining the two intervals yields the equation system

$$Ra_{c,3\text{-}D}(Ra_\theta, Re) = \begin{cases} Ra_{c,xy} \approx Ra_{c,0} + C_1 Re^2, & Re < Re_c, \\ Ra_{c,yz} = Ra_{c,0} - Ra_\theta, & Re \geqslant Re_c, \end{cases} \tag{3.7}$$

where $Re_c \approx \sqrt{-Ra_\theta / C_1}$, and $C_1 = 0.6$. The expression for Re_c shows that the transition between the two branches is governed jointly by Re and Ra_θ. Therefore, combining equation system (3.7) and figure 3(*a*) allows for effective prediction of whether the ACRBC system is in a stable state at large radius ratios under the current parameters (Re, Ra_θ, Ra).

4. Turbulent transport and flow structures in RSPCF

Having established the asymptotic connection between ACRBC and RSPCF through LSA, we now use RSPCF as the corresponding planar limiting system to investigate nonlinear turbulent transport. This section employs DNS to examine the nonlinear dynamical behaviour of the system in the turbulent regime, far from the critical point of instability. Our core objective is to test the universality of the twin-force analogy and the inertial-frame Reynolds analogy in complex turbulent environments, and to reveal the underlying physical mechanisms. The calculation results are presented in table 1. The discrepancies

https://doi.org/10.1017/jfm.2026.11999 Published online by Cambridge University Press

Re	Pr	$Ra/10^6$	R_Ω	Ri_χ	γ	Nu_T	Nu_θ	Nu_χ
10 000	1	1	−0.010	0	—	8.54	8.32	—
10 000	1	−1	0.010	0	—	8.49	8.56	—
10 000	1	−10	0.113	0	—	6.93	7.64	—
10 000	1	10	−0.092	0	—	9.61	8.06	—
10 000	1	20	−0.171	0	—	11.12	8.10	—
10 000	1	−20	0.276	0	—	5.11	5.91	—
10 000	1	0	0.000	0	—	8.47	8.39	—
10 000	1	−8	0.400	0.16	−2	13.40	14.33	14.80
10 000	1	0	0.200	0.16	−1	13.75	13.71	13.71
10 000	1	8	0.088	0.16	0	13.48	13.42	13.45
10 000	1	16	0.000	0.16	1	13.54	13.36	13.54
10 000	1	24	−0.074	0.16	2	14.60	14.07	14.86
5000	1	−1	0.042	0	—	4.71	4.91	—
5000	1	−2	0.088	0	—	4.40	4.71	—
5000	1	−6	0.400	0	—	2.06	1.65	—
5000	1	1	−0.039	0	—	5.35	5.12	—
5000	1	2	−0.074	0	—	5.72	5.17	—
5000	1	6	−0.200	0	—	7.42	5.42	—
5000	0.25	−2	0.400	0.16	−2	1.49	3.93	5.15
5000	0.25	0	0.200	0.16	−1	6.53	10.47	10.47
5000	0.25	2	0.088	0.16	0	7.32	11.70	9.51
5000	0.25	4	0.000	0.16	1	8.94	13.49	8.94
5000	0.25	5	−0.039	0.16	1.5	9.63	14.17	8.49
5000	4	−0.5	0.400	0.16	−2	17.64	10.52	9.87
5000	4	0	0.200	0.16	−1	16.88	10.47	10.47
5000	4	0.5	0.088	0.16	0	14.40	8.98	10.07
5000	4	1	0.000	0.16	1	9.68	5.38	9.68
5000	4	1.25	−0.039	0.16	1.5	6.71	3.48	19.63

Table 1. Summary of simulation parameters and results.

with Zhang & Sun (2024) arise from the non-uniqueness of the flow state. Specifically, variations in flow topology – manifested as differences in the number of dominant vortices – directly affect transport efficiency, which explains the relative deviations of approximately $O(5\,\%)$ in the reported statistics.

4.1. *Validation and breakdown of analogies at $Pr = 1$*

We first consider the most ideal case, $Pr = 1$. According to the prediction of the twin-force analogy, the overall transport efficiency of the system is primarily determined by the global Richardson number Ri_χ, and is independent of the specific ratio of rotation to stratification (Zhang & Sun 2024). A direct corollary is that when $Ri_\chi = 0$, regardless of the specific combination of the Coriolis force and buoyancy, the flow state should degenerate into ordinary plane Couette flow driven by shear. However, our DNS results reveal significant deviations from this prediction. As shown in figure 4, with fixed $Re = 10\,000$, $Pr = 1$, $Ri_\chi = 0$ and $Ra/10^6 = 0$, 1, −1, −10, 10, −20, 20, different combinations of rotation and stratification lead to distinct flow structures. When rotation acts to destabilise the flow (figure 4*a*), the flow evolves into ordered, nearly streamwise-homogeneous longitudinal vortices dominated by spanwise wavenumbers. It should be emphasised that the spanwise vortices identified in the preceding LSA and the streamwise-aligned longitudinal vortices observed here in the DNS correspond to different parameter regimes and are governed by

https://doi.org/10.1017/jfm.2026.11999 Published online by Cambridge University Press

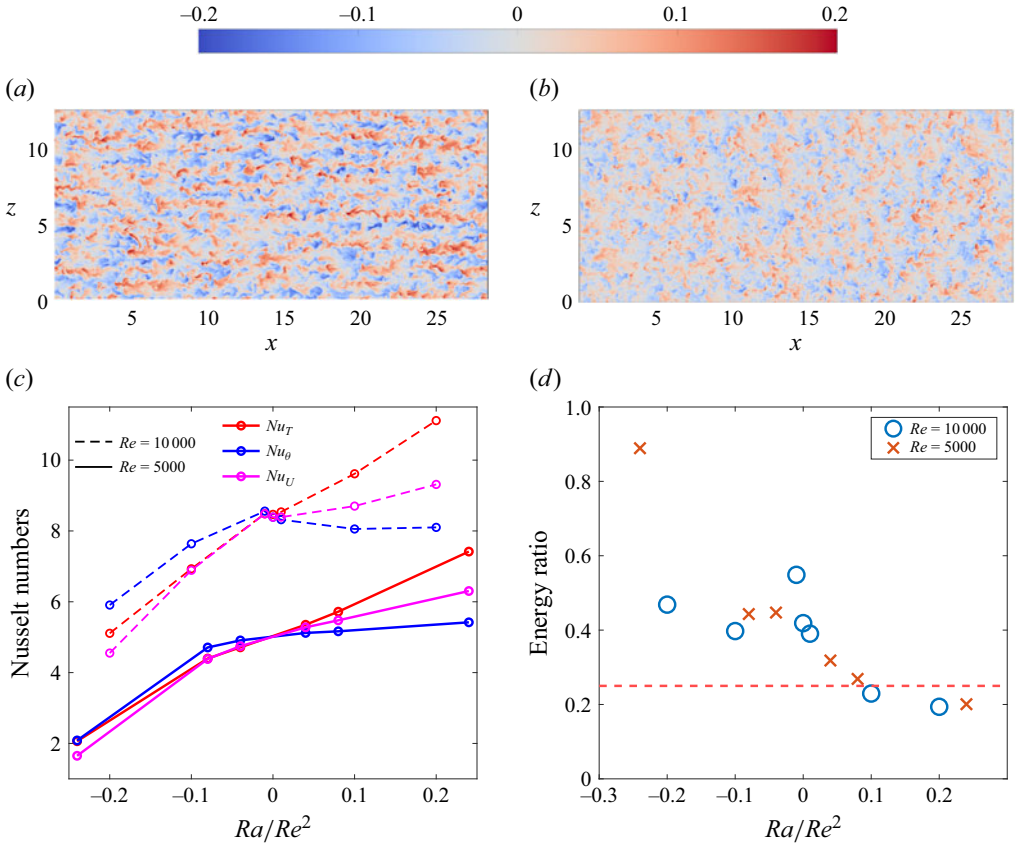


Figure 4. Results for $Re = 10\,000$, $Pr = 1$ under different rotation and stratification intensities with $Ra_\chi = 0$. (*a*,*b*) Temperature contours in the $x-z$ plane at $y = 0$ for $Ra/10^6 = -1$ and 20, respectively. (*c*) Corresponding Nusselt number results. (*d*) Energy fraction of the modes with $|\beta/\alpha| > 8$ for $Ra_\chi = 0$, $Re = 5000$ and 10 000 under different rotation and stratification intensities. The red dashed line marks the 25 % threshold.

different dominant mechanisms. Conversely, when buoyancy acts as the destabilising agent (figure 4*b*), the vortex structures are more chaotic, exhibiting small-scale features in both streamwise and spanwise directions.The differences in transport characteristics are equally significant; as shown in figure 4(*c*), when buoyancy effects are weak ($Ra \leqslant 10^6$), Nu_T and Nu_U are nearly identical, consistent with the classical Reynolds analogy, but differ slightly more from Nu_θ. However, in the strong destabilising buoyancy regime ($Ra > 10^6$), the thermal Nusselt number increases significantly with Ra, whereas the two momentum Nusselt numbers (influenced by the stabilising Coriolis force) show smaller variations, leading to the complete breakdown of both the classical Reynolds analogy and the inertial-frame Reynolds analogy.

Quantitative analysis of energy spectra (figure 4*d*) further confirms that the validity of the classical Reynolds analogy is closely related to the 'two-dimensionality' of the flow. We also verified six cases with $Re = 5000$, $Ra/10^6 = 1, -1, 2, -2, 6, -6$, and found that Nu_T and Nu_U exhibit similarity only when the energy fraction of structures characterised by a wavenumber ratio $|\beta/\alpha| > 8$ (explicitly including the $\alpha = 0$ mode) is relatively high – specifically, exceeding approximately 25 % (the red dashed line in figure 4*d*) in the present parameter space. The physical mechanism is that the flow field

https://doi.org/10.1017/jfm.2026.11999 Published online by Cambridge University Press

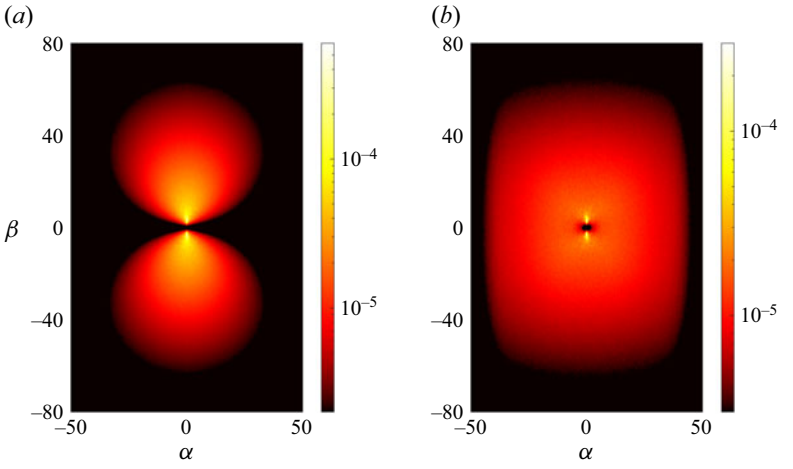


Figure 5. Spectral characteristics at $y = 0$ after virtually introducing buoyancy and rotation contributions to vorticity of plane Couette flow at $Re = 10\,000$: (*a*) rotation contribution; (*b*) buoyancy contribution.

exhibits significant quasi-two-dimensional characteristics. This streamwise homogeneity suppresses the three-dimensional effects that cause the discrepancy between momentum and scalar transport, thereby aligning their transport mechanisms. To analyse the effects of body forces on different modes, we define the buoyancy characteristic spectrum χ_b and the Coriolis force characteristic spectrum χ_c as follows:

$$\chi_b = (\alpha^2 + \beta^2)E_T, \quad \chi_c = \beta^2 E_k, \tag{4.1a,b}$$

where E_T and E_k are the squared moduli of the spectral coefficients for temperature and velocity, respectively. These definitions are based on the terms on the right-hand side of the vorticity equation derived by Zhang & Sun (2024). Figures 5(*a*,*b*) present the spectral signatures of vorticity contributions resulting from the virtual imposition of rotation and buoyancy effects upon a pure shear flow. The rotation-dominated case (refer to figure 4*a*) manifests strong anisotropy, with energy confined to a narrow band near $\alpha \approx 0$, and elongated along β, consistent with the potential spectral characteristics of the Coriolis force (figure 5*a*). In contrast, the flow field in the buoyancy-dominated regime (figure 4*b*) mirrors the buoyancy spectrum in figure 5(*b*), characterised by energy diffusion around the origin, and a broad distribution in both α and β directions. This suggests that thermal plume instability triggers complex three-dimensional, multi-scale motions. Consequently, unstable buoyancy promotes structural complexity, whereas the Coriolis force acts to organise the flow into coherent, anisotropic structures.

To fundamentally explain the impact of different driving forces on flow structure, we examined the budgets of the individual velocity-component contributions to turbulent kinetic energy (TKE) and enstrophy. The equation for the contribution of the ith velocity component to TKE is

$$\frac{\partial \langle k_{u_i} \rangle}{\partial t} + \langle u_j \rangle \frac{\partial \langle k_{u_i} \rangle}{\partial x_j} = -\langle u_i' u_j' \rangle \frac{\partial \langle u_i \rangle}{\partial x_j} - \frac{1}{Re} \left\langle \frac{\partial u_i'}{\partial x_j} \frac{\partial u_i'}{\partial x_j} \right\rangle + \frac{\partial}{\partial x_j} \left(\langle p' u_i' \rangle \delta_{ij} + \langle k_{u_i} u_j' \rangle + \frac{1}{Re} \frac{\partial \langle k_{u_i} \rangle}{\partial x_j} \right) + W_{C,u_i} + W_{B,u_i}, \tag{4.2}$$

https://doi.org/10.1017/jfm.2026.11999 Published online by Cambridge University Press

without summation over i, where $\phi' = \phi - \langle\phi\rangle$ denotes the fluctuating component of the variable ϕ. Here, $k_{u_i} = u_i' u_i'/2$ (no summation) represents the instantaneous contribution of the ith velocity component to the TKE; $\langle u_i' u_i'\rangle$ denotes the ith normal Reynolds stress component. The Coriolis force contribution is W_{C,u_i}, and the buoyancy contribution is W_{B,u_i}. The only non-zero terms of W_{B,u_i} and W_{C,u_i} are $W_{B,v} = (Ra/(Re^2 Pr))\langle v'T'\rangle$ and $W_{C,v} = -W_{C,u} = -R_\Omega \langle v'u'\rangle = Ri_\theta \langle v'\theta'\rangle$.

The work done by the Coriolis force appears only in the wall-normal and streamwise TKE equations, and since the Coriolis force does no net work, it serves only to transfer energy. As neither the Coriolis force nor buoyancy acts directly on the velocity field – requiring pressure projection to eliminate the longitudinal component (Zhang *et al.* 2020) – their forms in the vorticity equation are more fundamental. Therefore, one of the crucial tools for analysing the twin-force analogy is the enstrophy equation:

$$\begin{aligned}\frac{\partial\langle E_\omega'\rangle}{\partial t} + \langle u_j\rangle\frac{\partial\langle E_\omega'\rangle}{\partial x_j} + \frac{\partial\langle u_j' E_\omega'\rangle}{\partial x_j} = &-\left\langle u_j'\omega_i'\right\rangle\frac{\partial\langle\omega_i\rangle}{\partial x_j} + \langle\omega_j\rangle\left\langle\omega_i'\frac{\partial u_i'}{\partial x_j}\right\rangle + \left\langle\omega_i'\omega_j'\right\rangle\frac{\partial\langle u_i\rangle}{\partial x_j}\\ &+\left\langle\omega_i'\omega_j'\frac{\partial u_i'}{\partial x_j}\right\rangle + \frac{1}{Re}\frac{\partial^2\langle E_\omega'\rangle}{\partial x_j^2} - \frac{1}{Re}\left\langle\frac{\partial\omega_i'}{\partial x_j}\frac{\partial\omega_i'}{\partial x_j}\right\rangle\\ &+ E_B + E_C,\end{aligned} \tag{4.3}$$

where $\boldsymbol{\omega}$ represents the vorticity, $E_\omega' = \omega_i'\omega_i'/2$ is enstrophy, $E_B = -(Ra/(Re^2 Pr))\langle\omega_x'\,\partial T'/\partial z\rangle + (Ra/(Re^2 Pr))\langle\omega_z'\,\partial T'/\partial x\rangle$ is the buoyancy contribution, and $E_C = R_\Omega\langle\omega_x'\,\partial u'/\partial z\rangle + R_\Omega\langle\omega_y'\,\partial v'/\partial z\rangle + R_\Omega\langle\omega_z'\,\partial w'/\partial z\rangle$ is the Coriolis force contribution. Vorticity is the curl of the velocity field; when a material line element aligned with vorticity is stretched by velocity gradients, the magnitude of vorticity increases correspondingly due to the conservation of angular momentum, a process known as vortex stretching. The distinction between three-dimensional and two-dimensional flows is that the vortex stretching term is zero in two-dimensional flows. Notably, the formal similarity between the Coriolis force term and the vortex stretching term reveals the core mechanism by which system rotation affects vorticity dynamics.

To fundamentally reveal the physical mechanism underlying the breakdown of this analogy, we analysed the budgets of wall-normal TKE and enstrophy. Here, the enstrophy budget is used not as a direct measure of Nu_U, Nu_θ or Nu_T, but as a diagnostic of how buoyancy and Coriolis forces generate or maintain vortical structures that subsequently influence the associated turbulent fluxes. We first examine the case $Pr = 1$, systematically varying the relative strength of rotation and stratification under the condition that Ri_χ is non-zero. The energy budget analysis ultimately clarifies the root cause of the analogy's breakdown. In the wall-normal TKE equation, the two forces exhibit a misleading similarity: as shown by the solid lines in figure 6(*a*), when the contributions of buoyancy and the Coriolis force are consistent ($\gamma = 0$), their contribution profiles almost completely overlap. This overlap arises because at $Pr = 1$ and $\gamma = 0$, $Ri_\theta = Ri_T$ and the profiles of $\langle v'\theta'\rangle$ and $\langle v'T'\rangle$ are nearly identical. This explains why the two forces are analogous at the level of overall energy injection, leading to similarities in global transport coefficients. However, fundamental differences exist in the physical mechanisms of the two forces, which are vividly reflected in the enstrophy equation. In an ideal two-dimensional streamwise-homogeneous flow, the contribution terms of the Coriolis force and buoyancy to enstrophy are strictly symmetric in mathematical form, which would lead to a perfect inertial-frame Reynolds analogy. But in three-dimensional flow, this symmetry is broken: additional, asymmetric partial derivative terms appear in the buoyancy and Coriolis force contribution terms. This mathematical difference under three-dimensional effects leads

https://doi.org/10.1017/jfm.2026.11999 Published online by Cambridge University Press

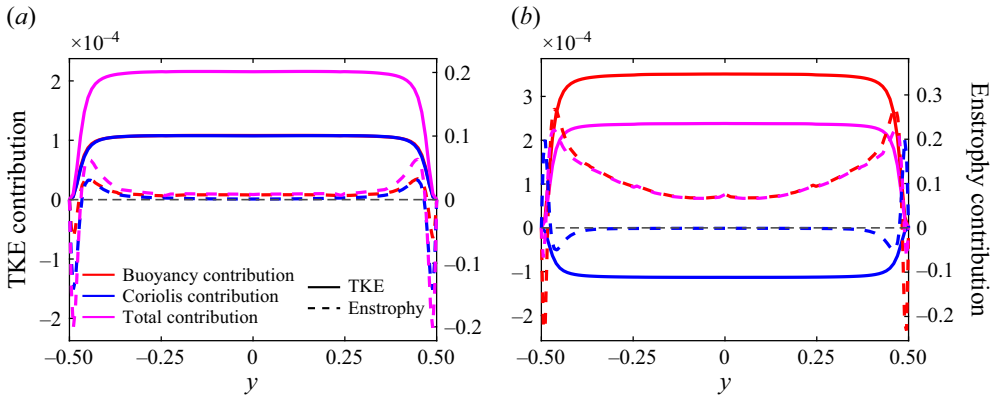


Figure 6. Contributions of buoyancy and Coriolis force in the enstrophy equation and wall-normal TKE equation for (*a*) $\gamma = 0$ and (*b*) $\gamma = 2$, respectively, at $Pr = 1$, $Re = 10\,000$, $Ra_\chi = 16 \times 10^6$. Red denotes buoyancy contribution, blue denotes Coriolis force contribution, and magenta denotes the net contribution between buoyancy and Coriolis force. Black is the reference line for zero. Solid lines represent contributions in wall-normal TKE, and dashed lines represent contributions in enstrophy.

to distinct spatial actions of the two forces (as shown by the dashed lines in figure 6*a*). The contribution of the Coriolis force to enstrophy is strictly concentrated in the near-wall region, whereas the contribution of buoyancy is distributed throughout the core region of the flow. Furthermore, as Ra increases (figure 6*b*), the vorticity generation mechanism dominated by buoyancy and acting in the flow core becomes increasingly important, causing the flow structure to further diverge from that under pure rotation, thereby exacerbating the deviation of transport coefficients.

Differences in flow structure directly affect the coherence of transport, leading to the breakdown of the inertial-frame Reynolds analogy. The root cause lies in the different ways in which buoyancy and the Coriolis force influence vorticity generation in three-dimensional space. The Coriolis force acts primarily in the spanwise direction, tending to generate longitudinal vortices aligned with the flow, lacking the modes dominated by streamwise wavenumbers found in buoyancy-driven convection. Such highly ordered vortex structures induced by the Coriolis force can bring about stronger ejection and sweep events, thereby generating Reynolds stresses more efficiently. This ultimately leads to an asymmetry between momentum transport correlation ($R_{v,-u}$) and heat transport correlation ($R_{v,T}$). Here, the correlation coefficient is defined as

$$R_{\xi_1,\xi_2} = \frac{\displaystyle\int_{-1/2}^{1/2} \langle \xi_1' \xi_2' \rangle \, \mathrm{d}y}{\sqrt{\displaystyle\int_{-1/2}^{1/2} \langle \xi_1'^2 \rangle \, \mathrm{d}y \int_{-1/2}^{1/2} \langle \xi_2'^2 \rangle \, \mathrm{d}y}}. \tag{4.4}$$

These correlation coefficients complement the Nusselt numbers by distinguishing changes in fluctuation amplitudes from changes in the correlation between the fluctuating fields. As shown in figure 7(*a*), in the Coriolis-dominated regime ($\gamma < 0$), the correlation coefficient $R_{v,-u}$ is enhanced. Conversely, in the buoyancy-dominated regime ($\gamma > 0$),$R_{v,T}$ becomes more prominent; this is because in an idealised state, the horizontally isotropic plume distribution statistically provides no net contribution to $\langle u'v' \rangle$.

https://doi.org/10.1017/jfm.2026.11999 Published online by Cambridge University Press

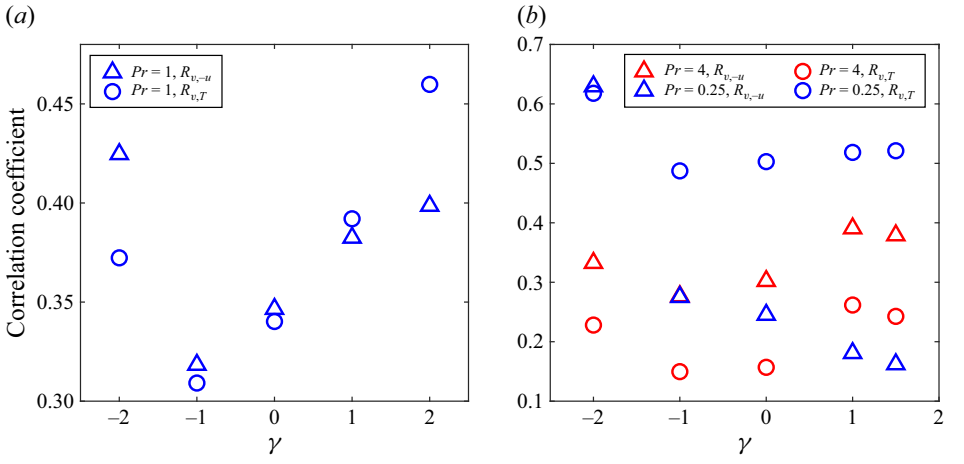


Figure 7. Comparison of correlation coefficients $R_{v,-u}$ and $R_{v,T}$: (*a*) $Pr = 1$, $Re = 10\,000$; (*b*) $Pr = 0.25$, 4 and $Re = 5000$. Both cases have fixed $Ri_\chi = 0.16$.

This mechanism fundamentally elucidates the results reported by Zhang & Sun (2024): specifically, under the condition $Pr = 1$, inertial-frame momentum transport is larger at $\gamma = -2$, while heat transport is larger at $\gamma = 2$.

4.2. *Extended analogy at different Prandtl numbers: symmetry breaking and transport dissimilarity*

When $Pr \neq 1$, the mismatch between heat and momentum diffusion rates leads to corrections to the perfect analogy observed at $Pr = 1$.

Various DNS results indicate that the transport properties systematically depend on Pr (Blass *et al.* 2021; Zhang & Sun 2024). For $Pr > 1$, the momentum boundary layer is thicker than the thermal boundary layer, making the flow more sensitive to the dynamical effects of rotation; consequently, both heat and momentum transport are enhanced as unstable rotation strengthens (decreasing γ). Conversely, for $Pr < 1$, the thermal boundary layer is thicker, rendering the flow more sensitive to the thermodynamic effects of buoyancy; thus transport efficiency increases with strengthening unstable stratification (increasing γ). Although the individual transport coefficients diverge, the modified global Nusselt number Nu_χ still exhibits a weak dependence within a certain range of γ. This symmetry breaking originates from the mismatch between the thermal and momentum boundary layer thicknesses at different Pr, which dictates the dominant spatial extent of buoyancy and Coriolis forces, respectively.

To quantitatively elucidate the turbulence structures and the underlying dynamic mechanisms, we combine quadrant analysis of the Reynolds stress-weighted joint probability density functions (at $y = -0.4$) with energy budget analysis. At $Pr = 0.25$, the energy budget analysis (figure 8) reveals that buoyancy makes significant contributions to both wall-normal TKE and enstrophy throughout the channel, whereas rotational effects are largely confined to the near-wall momentum boundary layer. This buoyancy-dominated driving force, acting over a broader spatial range, results in a more complex flow structure. The Reynolds stress quadrant analysis (Wallace 2016) (figure 9) provides direct evidence for this: for instance, under stable rotation ($\gamma = 1.5$; figure 9*b*), the negative contributions of inward/outward interaction events (Q1, Q3) to the Reynolds stress are significantly enhanced. This disrupts the coherence of momentum transport,

https://doi.org/10.1017/jfm.2026.11999 Published online by Cambridge University Press

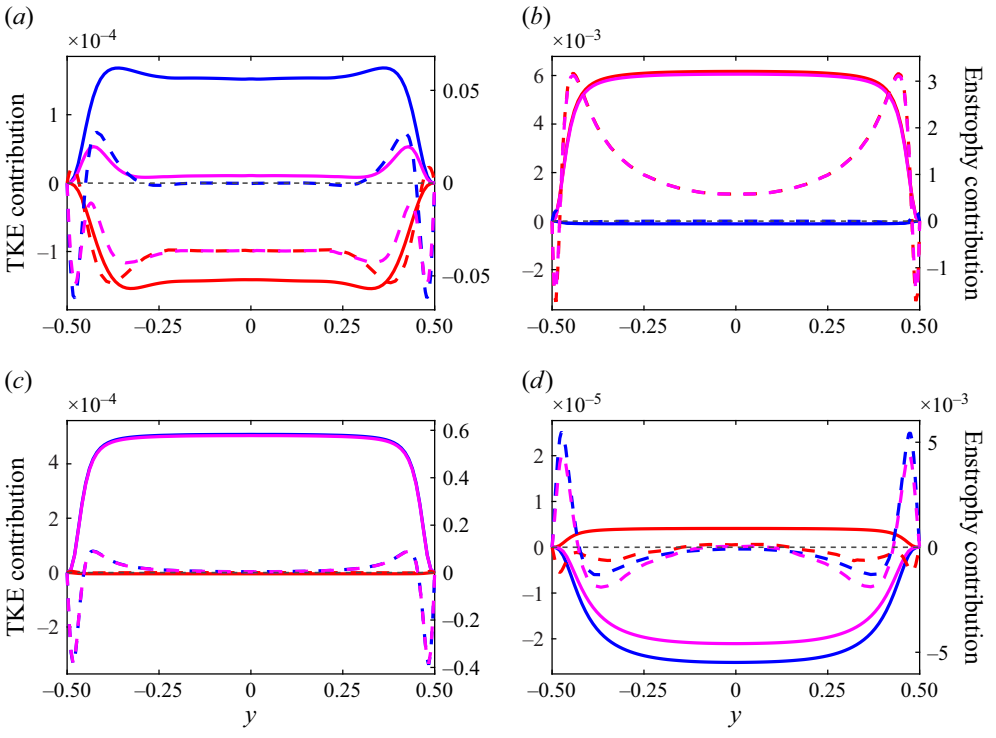


Figure 8. Contributions of buoyancy and Coriolis forces to the budgets of enstrophy and wall-normal TKE, for (*a*,*b*) $Pr = 0.25$ and (*c*,*d*) $Pr = 4$. The rotation ratios are (*a*,*c*) $\gamma = -2$ and (*b*,*d*) $\gamma = 1.5$. Red and blue lines denote the buoyancy and Coriolis force contributions, respectively. Solid and dashed lines represent contributions in wall-normal TKE and enstrophy, respectively.

leading to a reduction in $R_{v,-u}$ (figure 7*b*). In contrast, at $\gamma = -2$ (figure 8*a*), where the system is in the regime of unstable rotation and stable stratification, the thermal boundary layer is significantly thicker than the momentum boundary layer; consequently, the net contribution to enstrophy is negative, which also suppresses transport. The relatively high normalised correlations at $\gamma = -2$ do not contradict this suppression, because the turbulent fluxes also depend on the corresponding fluctuation amplitudes.

Conversely, at $Pr = 4$, the momentum boundary layer is thicker than the thermal one. At $\gamma = 1.5$ (figure 8*d*), energy budget analysis clearly demonstrates that the Coriolis contributions to wall-normal TKE and enstrophy far exceed those of buoyancy, with buoyancy effects confined to the extremely thin thermal boundary layer. Rotation acts to stabilise the flow; in the core region, it makes a significant negative contribution to both wall-normal TKE and enstrophy, leading to a drop in transport coefficients, with the flow tending towards a steady state at $\gamma = 2$ (Zhang & Sun 2024). The quadrant analysis for $\gamma = -2$ (figure 9*c*) confirms a flow field dominated by a single mechanical effect with a more organised structure, where ejection (Q2) and sweep (Q4) events dominate the Reynolds stress contribution. This organised Reynolds stress mechanism explains why the momentum–transport correlation is stronger than the heat–transport correlation across all $Pr = 4$ cases.

Therefore, when $Pr \neq 1$, the fundamental reason for the breakdown of the inertial-frame Reynolds analogy is that the Prandtl number, by controlling the relative thicknesses of thermal and momentum boundary layers, determines whether buoyancy or the Coriolis

https://doi.org/10.1017/jfm.2026.11999 Published online by Cambridge University Press

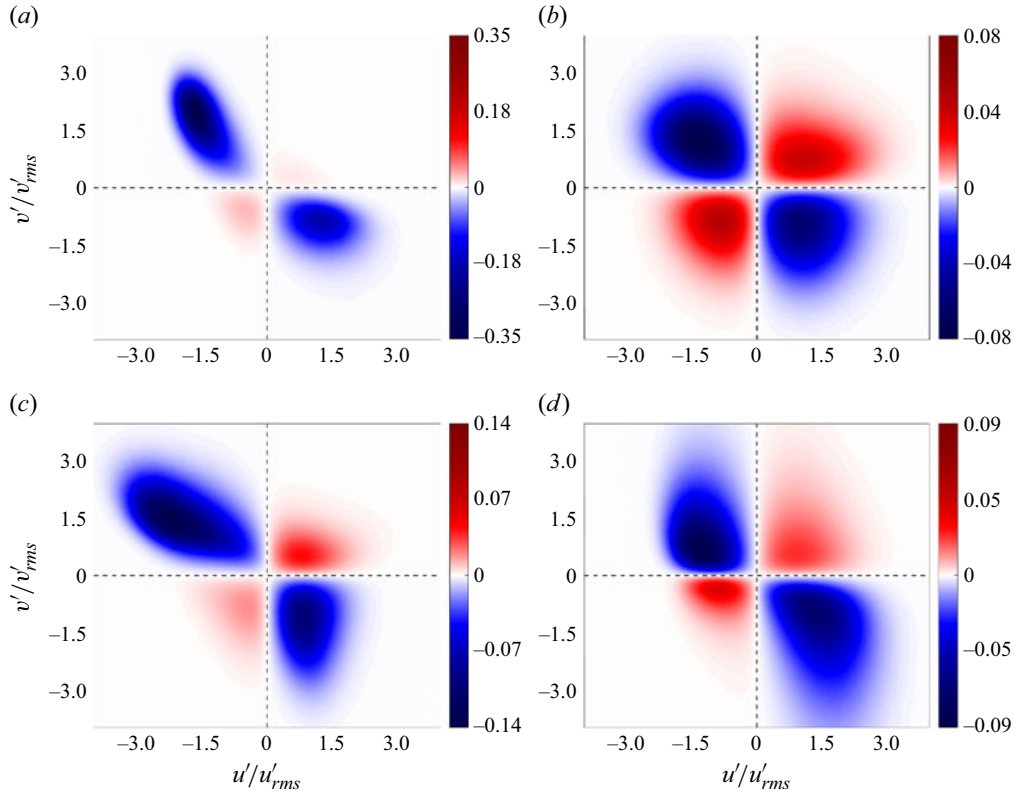


Figure 9. Reynolds-stress-weighted joint probability density functions $u'v'\,P(u', v')$ at $y = -0.4$, where $P(u', v')$ denotes the joint probability density function of the streamwise and wall-normal velocity fluctuations u' and v', respectively. The plotted variables are normalised by their respective root mean square (rms) values, for (a,b) $Pr = 0.25$ and (c,d) $Pr = 4$. The relative strength parameter is (a,c) $\gamma = -2$ and (b,d) $\gamma = 1.5$.

force dominates the flow field. Because these two forces differ significantly in the magnitude and spatial location of vorticity generation in three-dimensional space, they induce distinct turbulent structures, preventing a simple linear superposition of their effects.

5. Conclusion

The results of this study provide new theoretical insights into the physics of wall-bounded turbulence under coupled rotation, stratification and shear. Not only have we theoretically established a quantitative link between the complex annular centrifugal Rayleigh–Bénard convection and rotating stratified plane Couette flow systems via universal scaling laws of deviation with respect to $(1 - \eta)$, but more importantly, we have revealed the fundamental dynamic mechanism for the breakdown of the twin-force analogy in fully developed turbulence. The core lies in the intrinsic difference in how buoyancy and Coriolis forces support different types of flow modes in three-dimensional space, triggering modal competition. The destabilising Coriolis force tends to systematically suppress streamwise variations, promoting the development of quasi-two-dimensional, streamwise-aligned longitudinal vortices, which organise coherent ejection and sweep events associated with inertial-frame momentum transport. Conversely, buoyancy generates vorticity in

https://doi.org/10.1017/jfm.2026.11999 Published online by Cambridge University Press

both streamwise and spanwise directions via the baroclinic effect, tending to produce three-dimensional, asymmetric chaotic plumes that disrupt the symmetry required for momentum transport. The Prandtl number plays a decisive role in this competition. By regulating the relative thicknesses of thermal and momentum boundary layers, it determines whether thermodynamically driven buoyancy or mechanically driven Coriolis forces dominate the near-wall region, ultimately leading to the systematic separation of heat and inertial-frame momentum transport efficiencies. In summary, this study offers, for the first time, a clear dynamic explanation for the applicability boundaries of the twin-force analogy and its failure at $Pr \neq 1$ from the perspective of turbulence modal competition. The findings not only offer deeper understandings of how these two fundamental physical effects interact with shear, but also provide new physical insights and a theoretical basis for developing models to predict heat and momentum transport in complex industrial and geophysical flows.

Funding. This work was financially supported by the National Natural Science Foundation of China (grant nos 12302284 and U25A6006), the Ningbo Municipal Bureau of Education (grant no. 2024A-149-G), and the Ningbo Municipal Bureau of Science and Technology (grant nos 2023Z227 and 2023-DST-001).

Declaration of interests. The authors report no conflict of interest.

References

Ahlers, G., Grossmann, S. & Lohse, D. 2009 Heat transfer and large scale dynamics in turbulent Rayleigh–Bénard convection. *Rev. Mod. Phys.* **81** (2), 503–537.

Blass, A., Tabak, P., Verzicco, R., Stevens, R.J.A.M. & Lohse, D. 2021 The effect of Prandtl number on turbulent sheared thermal convection. *J. Fluid Mech.* **910**, A37.

Blass, A., Zhu, X., Verzicco, R., Lohse, D. & Stevens, R.J.A.M. 2020 Flow organization and heat transfer in turbulent wall sheared thermal convection. *J. Fluid Mech.* **897**, A22.

Brauckmann, H.J., Eckhardt, B. & Schumacher, J. 2017 Heat transport in Rayleigh–Bénard convection and angular momentum transport in Taylor–Couette flow: a comparative study. *Phil. Trans. R. Soc. Lond. A: Math. Phys. Engng Sci.* **375** (2089), 20160079.

Brauckmann, H.J., Salewski, M. & Eckhardt, B. 2016 Momentum transport in Taylor–Couette flow with vanishing curvature. *J. Fluid Mech.* **790**, 419–452.

Brethouwer, G. 2018 Passive scalar transport in rotating turbulent channel flow. *J. Fluid Mech.* **844**, 297–322.

Brethouwer, G. 2021 Much faster heat/mass than momentum transport in rotating Couette flows. *J. Fluid Mech.* **912**, A31.

Brethouwer, G. 2023 Strong dissimilarity between heat and momentum transfer in rotating Couette flows. *Intl J. Heat Mass Transfer* **205**, 123920.

Busse, F.H. 2012 The twins of turbulence research. *Physics* **5**, 4.

Chandrasekhar, S. 1961 *Hydrodynamic and Hydromagnetic Stability*. Clarendon Press.

Deardorff, J.W. 1972 Numerical investigation of neutral and unstable planetary boundary layers. *J. Atmos. Sci.* **29** (1), 91–115.

Dou, H.-S., Khoo, B.C. & Yeo, K.S. 2008 Instability of Taylor–Couette flow between concentric rotating cylinders. *Intl J. Therm. Sci.* **47** (11), 1422–1435.

Eckhardt, B., Doering, C.R. & Whitehead, J.P. 2020 Exact relations between Rayleigh–Bénard and rotating plane Couette flow in two dimensions. *J. Fluid Mech.* **903**, R4.

Etling, D. & Brown, R.A. 1993 Roll vortices in the planetary boundary layer: a review. *Boundary-Layer Meteorol.* **65** (3), 215–248.

Faisst, H. & Eckhardt, B. 2000 Transition from the Couette–Taylor system to the plane Couette system. *Phys. Rev. E* **61** (6), 7227.

Feng, L., Liu, C., Köhl, A. & Wang, F. 2022 Seasonality of four types of baroclinic instability in the global oceans. *J. Geophys. Res.: Oceans* **127** (5), e2022JC018572.

Goluskin, D., Johnston, H., Flierl, G.R. & Spiegel, E.A. 2014 Convectively driven shear and decreased heat flux. *J. Fluid Mech.* **759**, 360–385.

Grossmann, S. & Lohse, D. 2001 Thermal convection for large Prandtl numbers. *Phys. Rev. Lett.* **86** (15), 3316.

https://doi.org/10.1017/jfm.2026.11999 Published online by Cambridge University Press

GROSSMANN, S. & LOHSE, D. 2002 Prandtl and Rayleigh number dependence of the Reynolds number in turbulent thermal convection. *Phys. Rev. E* **66** (1), 016305.
GROSSMANN, S., LOHSE, D. & SUN, C. 2016 High–Reynolds number Taylor–Couette turbulence. *Annu. Rev. Fluid Mech.* **48** (1), 53–80.
HARTMANN, D.L., MOY, L.A. & FU, Q. 2001 Tropical convection and the energy balance at the top of the atmosphere. *J. Clim.* **14** (24), 4495–4511.
HATHAWAY, D.H. & SOMERVILLE, R.C.J. 1986 Nonlinear interactions between convection, rotation and flows with vertical shear. *J. Fluid Mech.* **164**, 91–105.
JEGANATHAN, V., ALBA, K. & OSTILLA-MÓNICO, R. 2023 Exploring the origin of turbulent Taylor rolls. *Phil. Trans. R. Soc. Lond. A: Math. Phys. Engng Sci.* **381**, 20220130.
KANG, C., MEYER, A., YOSHIKAWA, H.N. & MUTABAZI, I. 2019 Numerical study of thermal convection induced by centrifugal buoyancy in a rotating cylindrical annulus. *Phys. Rev. Fluids* **4** (4), 043501.
TANAKA, M., KIDA, S., YANASE, S. & KAWAHARA, G. 2000 Zero-absolute-vorticity state in a rotating turbulent shear flow. *Phys. Fluids* **12** (8), 1979–1985.
WALLACE, J.M. 2016 Quadrant analysis in turbulence research: history and evolution. *Annu. Rev. Fluid Mech.* **48** (1), 131–158.
WALLIN, S., GRUNDESTAM, O. & JOHANSSON, A.V. 2013 Laminarization mechanisms and extreme-amplitude states in rapidly rotating plane channel flow. *J. Fluid Mech.* **730**, 193–219.
WYNGAARD, J.C. 1992 Atmospheric turbulence. *Annu. Rev. Fluid Mech.* **24** (1), 205–234.
YOSHIKAWA, H.N., NAGATA, M. & MUTABAZI, I. 2013 Instability of the vertical annular flow with a radial heating and rotating inner cylinder. *Phys. Fluids* **25** (11), 114104.
YOUNG, R.M.B. & READ, P.L. 2017 Forward and inverse kinetic energy cascades in Jupiter's turbulent weather layer. *Nat. Phys.* **13** (11), 1135–1140.
ZHANG, S. & SUN, C. 2024 Twin forces: similarity between rotation and stratification effects on wall turbulence. *J. Fluid Mech.* **979**, A45.
ZHANG, S., XIA, Z. & CHEN, S. 2022 Perturbation analysis of baroclinic torque in low-Mach-number flows. *J. Fluid Mech.* **930**, A4.
ZHANG, S., XIA, Z., SHI, Y. & CHEN, S. 2019 A two-dimensional-three-component model for spanwise rotating plane Poiseuille flow. *J. Fluid Mech.* **880**, 478–496.
ZHANG, S., XIA, Z., ZHOU, Q. & CHEN, S. 2020 Controlling flow reversal in two-dimensional Rayleigh–Bénard convection. *J. Fluid Mech.* **891**, R4.
ZHONG, J., LI, J. & SUN, C. 2024 Effect of radius ratio on the sheared annular centrifugal turbulent convection. *J. Fluid Mech.* **992**, A16.
ZHONG, J., WANG, D. & SUN, C. 2023 From sheared annular centrifugal Rayleigh–Bénard convection to radially heated Taylor–Couette flow: exploring the impact of buoyancy and shear on heat transfer and flow structure. *J. Fluid Mech.* **972**, A29.

https://doi.org/10.1017/jfm.2026.11999 Published online by Cambridge University Press